# *THE EFFECT OF ARM THICKNESS ON THE FLOW INDUCED HEAD VIBRATION BETWEEN CO-ROTATING DISKS*

***Toru Watanabe***

***HDD Division, Fujitsu Ltd.***

***4-4-1 Kamikodanaka, Nakahara-ku,***

***Kawasaki, 211-8588, Japan***

***Hany M. Gross and David B. Bogy***

***Computer Mechanics Laboratory***

***Department of Mechanical Engineering***

***University of California, Berkeley 94720***

## *Abstract*

*In this work, flow induced off-track vibration of the read/write head between co-rotating disks was investigated experimentally. In particular, the effect of E-block arm thickness on the head off-track vibration was investigated in a modeled disk drive prepared for this study. Four different E-block arm thicknesses were used, ranging from 1.0 mm to 1.6 mm in steps of 0.2 mm. Two head gimbal assemblies were attached to each E-block arm, and they were inserted between co-rotating disks, rotating at 10,000 RPM, and fixed at a disk spacing of 2.0 mm. Head vibration in the off-track direction was measured using a laser Doppler vibrometer at the inner diameter, the middle diameter, and the outer diameter positions. The frequency range considered was 2-20 kHz. Finite element analysis was used to compute the natural frequencies and mode shapes of the head gimbal assembly, the E-block arms, and the head stack assemblies, in order to identify the resonances observed in the experimental measurements.*

*The primary contributors to the measured head off-track vibration were identified as the E-block arm sway mode, the suspension second torsion mode, and the suspension sway mode. The off-track RMS amplitude was determined over three frequency bands in the measurement range in order to isolate the contributions of the E-block arm vibration and the suspension vibration to off-track RMS amplitude.*

## *Table of Contents*

## *List of Tables*

## *List of Figures*

## *1. Introduction*

The hard disk drive (HDD) industry is faced with demands for higher areal recording densities, faster data transfer rates, and a higher reliability. The areal recording density can be increased by increasing the track density and the linear bit density. Track densities beyond 40,000 tracks per inch (TPI) have already been implemented in current drives, and higher density objectives have made their way into industry roadmaps. Track misregistration (TMR) must be reduced in order to achieve such high track densities. On the other hand, the demand for higher data transfer rates has resulted in higher disk rotation speeds, which, in turn, has lead to higher flow velocities that increased aerodynamic forces in the drive. These forces excite the head gimbal assemblies (HGA) and the E-block arms, leading to head off-track vibration.

Early research on the effects of air flow in hard disk drives on suspension vibration was carried out by Yamaguchi *et al.* [1]. The findings in [1] indicated that the amplitude of suspension vibration was proportional to the square of the approaching velocity. In subsequent research by Yamaguchi *et al.* [2, 3], the flow around a suspension was measured using hot-wire anemometry to identify the sources of suspension vibration, and numerical simulations of the flow were carried out. It was shown in [2, 3] that suspension vibration was caused by the turbulence behind the suspension cross-section, and that applying an aerofoil shape to the suspension cross-section can reduce suspension vibration.

The flow field between co-rotating disks that are fully shrouded by a cylindrical wall was numerically investigated by Iglesias *et al.* [4]. The research in [4] concluded that there were significant vertical velocity fluctuations at the disk outer region, which resulted in disk flutter. The presence of the E-block arm between the disks in an actual disk drive gives rise to a more complicated flow structure, which prompts an investigation of the effects of the arm to the flow between disks. Abrahamson *et al.* [5] performed flow visualization experiments using a dye method on a modeled realistic disk drive, but without considering the effects of the HGA. Vortex shedding from the arm tip was observed. Harrison *et al.* [6] measured the flow field around an arm using hot-wire anemometry. It was shown that the mean flow velocity increased as the disks were shrouded and/or as the disk spacing was decreased. A numerical investigation of the flow around the arm was performed with Suzuki *et al.* [7]. They showed that the insertion of the arm between co-rotating disks causes disk flutter and power losses due to windage.

A transverse type arm was used in the studies carried out in [4, 5, 6, 7]. Current disk drives, however, employ in-line type arm/suspension assemblies. Flow visualization experiments for in-line type arm/suspension assemblies were carried out by Girard *et al.* [8]. Vortex shedding around the arm tip was observed. However, the flow-induced vibration of the E-block arm and the suspension and its associated effects on TMR were not investigated.

In this study, flow induced off-track vibration of the read/write head between co-rotating disks was investigated experimentally. In particular, the effect of E-block arm thickness on the head off-track vibration was investigated in a modeled drive, prepared for this work. Four different E-block arm thicknesses were used, ranging from 1.0 mm to 1.6 mm in steps of 0.2 mm. Two HGAs were attached to each E-block arm, and they were inserted between co-rotating disks, rotating at 10,000 RPM, and fixed at a disk spacing of 2.0 mm. Head vibration in the off-track direction was measured using a laser Doppler vibrometer at three radial positions: the inner diameter (ID), the middle diameter (MD), and the outer diameter (OD). The frequency range considered was 2-20 kHz. Finite element analysis (FEA) was used to compute the natural frequencies and mode shapes of the HGA, the E-block arms, and the head stack assemblies (HSA), in order to identify the resonances observed in the experimental measurements.

## *2. Experimental Setup*

The modeled drive shown in Fig. 1 was prepared for this study. The setup consists of a fixed plate A, to which the E-block is completely fixed using a screw; and a movable plate B, on which is mounted the spindle, the shroud, and the rest of the enclosure. The E-block, shown in Fig.2, does not have a pivot and a coil, and it does not rotate to seek different radial positions on the disks. Instead, the head is positioned at different radial positions by rotating plate B, and consequently the spindle and disks, about the axis that corresponds to the actual pivot of the E-block. The precision of positioning the head at the ID, MD, and OD is achieved through the use of pins that fit in carefully positioned holes on plate A. This arrangement was used in order to allow for changing the radial position of the head without changing the relative position between the head and the air table on which the experiment was mounted. This was very convenient for measuring the head vibration using a laser Doppler vibrometer (LDV) since it eliminated the need to re-adjust the LDV cable to re-establish beam alignment and focus.

The spindle used in the setup was an actual drive ball bearing spindle, and it was operated at 10,000 RPM in this study. In the operating state, the rotating disks were covered by a glass plate, as shown in Fig. 1(b). A cross plate - marked in the figure - was used to support the spindle at the top to reduce spindle vibrations. Fujitsu's pico-CAPS suspensions for pico-sliders (Fig. 3) were used in this experiment. The loadbeam cross section of the pico-CAPS suspension is rectangular, and is flangeless. Four different E-block arm thicknesses were tested: 1.0 mm, 1.2 mm, 1.4 mm and 1.6 mm. Two HGAs were attached, using an adhesive, to each arm, and were inserted between two 84 mm diameter platters, at a disk spacing of 2.0 mm. A POLYTEC OFV-1102 LDV was used for taking the measurements, and its output was fed to an HP3562A signal analyzer to obtain the power spectra. The slider off-track vibration was measured at the ID, MD, and OD, for each of the arm thicknesses above, giving a total of twelve measurement sets. For each arm thickness, all measurements were repeated on two identical HSA samples to ensure consistency of the results.

## 3. Finite Element Modeling and Analysis

### 3.1. Head Gimbal Assembly

The pico-CAPS HGA was modeled in ANSYS as shown in Fig. 4. The baseplate, loadbeam, and slider were modeled using SOLID45 3-D structural solid elements. MASS21 structural mass elements were used to model the trace and damping layers on the suspension, the flexible printed circuit terminal, and the gold balls used to ensure electrical connection between the slider and the trace. The position of the terminal is not the same for the upper and lower HGAs. ANSYS modal analysis was used to compute the natural frequencies and associated mode shapes of the active modes of the upper and lower HGAs in the 0-20 kHz frequency range. The results are presented in Table 1.

### 3.2. E-Block Arm

The E-block arm was modeled in ANSYS as shown in Fig. 5. The arm was modeled using SOLID45 3-D structural solid elements. The natural frequencies and associated mode shapes of the E-block arm were computed using ANSYS modal analysis for each arm thickness. The results are presented in Table 2 for the first five modes. The variation of the natural frequencies of these modes as a function of E-block arm thickness is shown in Fig. 6. Note that the natural frequency of the sway mode is less sensitive to the change in arm thickness than the natural frequencies of the other modes.

### *3.3. Head Stack Assembly*

The HSA in this study consisted of a single E-block arm and two HGAs. The HSA was modeled by combining the component models described above, as illustrated in Fig. 7. The natural frequencies and associated mode shapes of the HSA were obtained using ANSYS modal analysis for each arm thickness. The HSA active modes in the 0-20 kHz range are numerous due to the dynamic coupling between the upper and lower HGA modes, and the dynamic coupling between the HGA modes and the E-block arm modes. A complete list of these modes is not provided. Table 3 lists the FEA results for the natural frequencies and mode shapes of the HSA modes that were identified in the experimental measurements. The first mode listed in Table 3 is dominated by the E-block arm sway mode, which drives the suspension sway mode. It should be noted that the slope of variation of natural frequency of this mode is roughly the same as that of the natural frequency of the E-block arm sway mode presented in section 3.2. This is illustrated in Fig. 8.

## *4. Results and Discussion*

The power spectra of the slider off-track vibration for the different arm thicknesses are shown in Figs. 9 through 12. All of these spectra exhibit three dominant resonance peaks, the frequencies for which are listed in Table 4. The first resonance peak occurred at a frequency of around 8 kHz, and was identified as the E-block arm sway coupled with the suspension sway mode (the first mode in Table 3). The discrepancy between the frequencies computed using FEA and those obtained experimentally can be attributed to the incompleteness and simplicity of the FE model. Nonetheless, the congruence of the slope of variation of the frequency of the measured resonance and that of the natural frequency of the E-block arm sway/suspension sway mode presented in section 3.3 is a clear indicator that the observed mode is, in fact, the identified one (Fig.8).

The second and third major resonance peaks in the measured spectra occurred at frequencies around 12 kHz and 14 kHz, respectively. The 12 kHz resonance peak was identified as the second torsion mode of the HGA; the 14 kHz resonance peak was identified as the sway mode of the HGA. Note that the frequencies of these two peaks are relatively insensitive to changes in the E-block arm thickness. The power spectrum of the slider off-track vibration for the 1.0 mm thick E-block arm (Fig. 9) also contains two small peaks at 2.65 kHz and 5.7 kHz. The former peak is the first bending mode of the HGA, and the latter is the base plate first bending coupling with the HGA second bending mode. The amplitude of the 2.65 kHz peak is more than 10 dB lower than the three major modes in the spectra, and the amplitude of the 5.7 kHz peak is 20 dB lower than the three major modes in the spectra. Consequently, the contributions of these two modes to the slider off-track motion are relatively small.

The root mean square (RMS) amplitude of the slider off-track vibration was evaluated for each E-block arm thickness over the 2-20 kHz frequency range. These RMS amplitudes are listed in Table 5 and are plotted in Fig. 13. These RMS amplitudes were then broken down into components in the 2-6 kHz, 6-10 kHz, and 10-20 kHz frequency bands in order to assess the contributions resulting primarily from suspension vibration (2-6 kHz and 10-20 kHz bands), and those resulting primarily from E-block arm vibration (6-10 kHz band). These RMS amplitude components are listed in Tables 6 through 8 and are plotted in Figs. 14 through 16.

A common feature of all the off-track vibration power spectra is that the amplitude of the slider off-track vibration increased as the slider was moved from the ID to the MD to the OD. This is clearly evident in Fig. 13. An examination of the component plots in Figs. 14 through 16 indicates that this phenomenon is true for all components as well, and is most pronounced for the suspension second torsion and sway modes, which are captured in the 10-20 kHz frequency band.

The first torsion mode of the HGA occurs at around 4 kHz, but there is no peak at this frequency in the any of the power spectra, which indicates that this mode is not excited significantly. This explains the lack of dependency of the RMS amplitude components in the 2-6 kHz frequency band on arm thickness, as evident from Fig. 14.

Figure 15 indicates that the RMS amplitude components in the 6-10 kHz frequency band are dependent on arm thickness. The main mode excited in this frequency band is the sway mode of the E-block arm, which occurs at around 8 kHz. Going from the 1.0 mm thick arm to the 1.2 mm thick arm, the RMS amplitude components in Fig. 15

attain their highest values at the 1.2 mm thickness and then decrease to attain their lowest values at the 1.6 mm thickness for all radial positions. This phenomenon is quite interesting, and can be explained as the combination of two effects. The first effect can be explained by noting that if the same external forces are applied to each E-block arm, then the amplitude of the arm sway mode must decrease as arm thickness increases, due to the increase in inertia that accompanies the increase in arm thickness. This explains the decline in amplitude observed going from the 1.2 mm arm thickness to the 1.6 mm arm thickness.

The increase in the RMS amplitude components observed in the 6-10 kHz frequency band as the arm thickness goes from 1.0 mm to 1.2 mm is explained by the second effect, which is the increase in the drag force as the arm thickness increases. In general, the drag force $D$ is proportional to the square of the flow velocity, and can be expressed in terms of the fluid density $r$, the flow velocity $U$, the area $S$ normal to the flow, and the drag coefficient $C_D$, as

$$D = \tfrac{1}{2} r U^2 S C_D \qquad (1).$$

In the case at hand, where the arm is inserted between two disks, the drag force can be broken down into a friction drag force, and a pressure drag force. The friction drag $D_f$ and the pressure drag $D_p$ can be expressed as

$$D_f = \int_A \hat{o}\, dA \qquad (2),$$

$$D_p = \int_S p\, dS \qquad (3),$$

where $t$ is the shear stress, $p$ is the pressure, and $A$ is the area parallel to the flow.

Reynolds number *Re*, defined by

$$Re = \frac{Uh}{\acute{\imath}} \qquad (4),$$

was computed at the OD for all arms (listed in Table 9), using the speed at the outer disk, $U = 44\ m/s$, the kinematic viscosity of air, $n = 1.512 \times 10\text{-}5\ m^2/s$, and the appropriate distance between the arm surface and the disk, $h$. Since *Re* was lower than 2000 for all arms, the flow between the arm and the disk can be assumed to be a Couette flow and the shear stress $t$ is expressed by

$$\hat{o} = \grave{\imath}\ \frac{U}{h} \qquad (5),$$

where $m$ is the fluid static viscosity. Increasing the arm thickness results in a smaller spacing $h$ between the arm surface and the disk and an increased area $A$ parallel to the flow, which leads to a higher shear stress according to Eq. (5), and that in turn leads to a higher friction drag $D_f$ according to Eq. (2). Increasing the arm thickness also results in an increased area $S$ normal to the flow, which leads to a higher pressure drag force $D_p$, according to Eq. (3). Consequently, increasing the E-block arm thickness yields a higher drag force, and that produces higher levels of vibration.

The variation of the RMS amplitude components in the 10-20 kHz band (Fig. 16) as a function of E-block arm thickness follows a similar trend to that observed for the RMS amplitude components in the 6-10 kHz band, although the effect is on a much smaller scale. This trend is a result of the dynamic coupling between the E-block arm and the suspensions.

The variation of the RMS amplitude of the slider off-track vibration over the 2-20 kHz frequency range as a function of E-block arm thickness is primarily shaped by the 6-10 kHz component, as evident from Figs. 13 and 15.

## *5. Conclusion*

In this study, the effect of E-block arm thickness on the off-track vibration of a read/write head inserted between two co-rotating disks was investigated experimentally in a modeled disk drive. Four different E-block arm thicknesses were used, ranging from 1.0 mm to 1.6 mm in steps of 0.2 mm. Head vibration in the off-track direction was measured at the inner diameter, the middle diameter, and the outer diameter positions. For each E-block arm thickness, the head exhibited the highest level of off-track vibration at the outer diameter, and the lowest level of off-track vibration at the inner diameter.

The primary contributors to the measured off-track vibration were identified as the E-block arm sway mode, the suspension second torsion mode, and the suspension sway mode. The off-track RMS amplitude was broken down into components over three frequency bands in the measurement range in order to isolate the contributions of the E-block arm vibration and the suspension vibration to off-track RMS amplitude.

The measured off-track RMS amplitude was dependent on the E-block arm thickness. The RMS amplitudes, for all radial positions, increased as the arm thickness was increased to attain their highest values at the 1.2 mm arm thickness, and then decreased as the arm thickness was increased further to attain their lowest values at the 1.6 mm thickness. This trend in the observed off-track vibration was strongly shaped by the component of off-track resulting from the E-block arm vibration, and was explained by the change in the E-block arm inertia and the change in the drag force that accompany the change in arm thickness.

## *6. References*


[1] Yamaguchi, Y., Takahashi, K., Fujita, H. and Kuwahara, K., "Flow Induced Vibration of Magnetic Head Suspension in Hard Disk Drive", IEEE Transaction on Magnetics, Vol. 22, No. 5, September 1986, pp. 1022-1024.

[2] Tokuyama, M., Yamaguchi, Y., Miyata, S. and Kato, C., "Numerical Analysis of Flying-Height Fluctuation and Positioning Error of Magnetic Head due to Flow Induced by Disk Rotation", IEEE Transaction on Magnetics, Vol. 27, No. 6, November 1991, pp. 5139-5141.

[3] Abrahamson, S., Chiang, C. and Eaton, J.K., "Flow Structure in Head-Disk Assemblies and Implications for Design", Advanced Information Storage Systems, Vol. 1, 1991, pp. 111-132.

[4] Harrison, J.C., Lou, D.H. and Talke, F.E., "AirFlow at the Tip of an Obstruction Between Corotaing Disks", Advanced Information Storage Systems, Vol. 5, 1993, pp. 159-174.

[5] Girard, J., Abrahamson, S. and Uznanski, K., "The Effect of Rotary Arms on Corotating Disk Flow", ASME Journal of Fluids Engineering, Vol. 117, June 1995, pp. 259-262.

[6] Suzuki, H. and Humphrey, J., "Flow Past Large Obstructions Between Corotating Disks in Fixed Cylindrical Enclosures", ASME Journal of Fluids Engineering, Vol. 119, September 1997, pp. 499-505.

[7] Iglesias, I. and Humphrey, J., "Two- and Three-Dimensional Laminar Flows Between Disks Co-Rotating in a Fixed Cylindrical Enclosure", International Journal for Numerical Methods in Fluids, Vol. 26, 1998, pp. 581-603.

## *Acknowledgements*

This study was supported by the Computer Mechanics Laboratory at the University of California at Berkeley and by the HDD Division at Fujitsu Ltd.

| Natural Frequency [Hz] | | Mode Shape | |
| --- | --- | --- | --- |
| Upper | Lower | | |
| 2,202 | 2,202 | Loadbeam first bending | 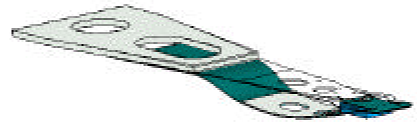 |
| 4,078 | 4,078 | Loadbeam first torsion |  |
| 5,470 | 5,518 | Baseplate first bending in phase with loadbeam second bending | 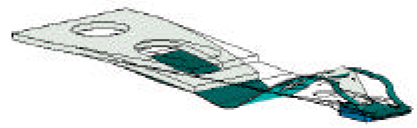 |
| 6,937 | 7,049 | Baseplate first bending out of phase with loadbeam second bending | 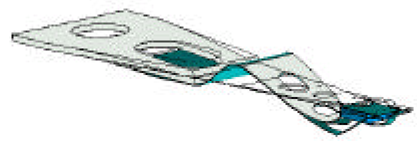 |
| 12,955 | 12,955 | Loadbeam second torsion | 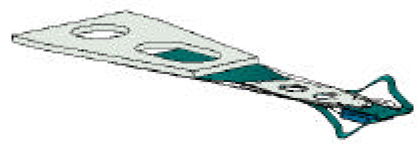 |
| 13,095 | 13,080 | Loadbeam third bending |  |
| 14,421 | 14,417 | Loadbeam sway | 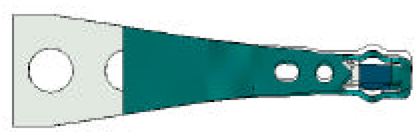 |
| 18,547 | 18,544 | Loadbeam fourth bending | 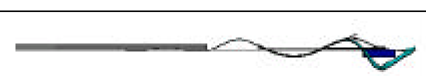 |
| 19,069 | 17,350 | Loadbeam third torsion in phase with baseplate first torsion | 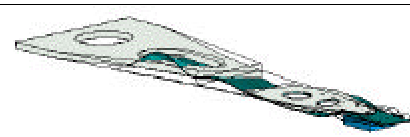 |
| 20,127 | 19,790 | Loadbeam third torsion out of phase with baseplate first torsion | 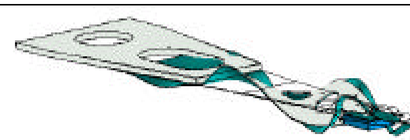 |

Table 1: HGA natural frequencies and mode shapes of active modes in 0-20 kHz range.

| Natural Frequency [Hz] | | | | Mode Shape | |
|---|---|---|---|---|---|
| **t = 1.0** | **t = 1.2** | **t = 1.4** | **t = 1.6** | | |
| 2007.1 | 2499.9 | 2999.4 | 3502.7 | First bending |  |
| 9155.5 | 11015 | 12809 | 14515 | Second bending | 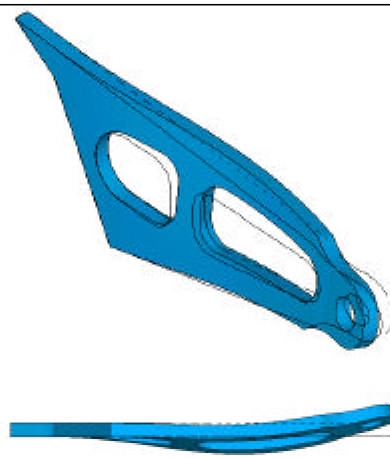 |
| 11235 | 13343 | 15400 | 17415 | First torsion | 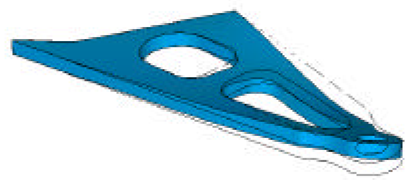 |
| 13860 | 14285 | 14610 | 14867 | Sway | 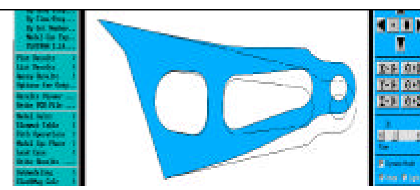 |
| 22971 | 27237 | 31266 | 35025 | Third bending |  |

Table 2: E-block arm natural frequencies and mode shapes of first five modes.

| Mode Shape | Natural Frequencies [Hz] | | | |
|---|---|---|---|---|
| | t =1.0 | t =1.2 | t =1.4 | t =1.6 |
| E-block sway coupled with suspension sway | 9196.0 | 9721.3 | 10149 | 10503 |
| E-block first torsion coupled with suspension third bending | 9119.5 | 10447 | 11508 | 13421 |
| Suspension second torsion (upper and lower suspensions in phase) | 12960 | 12972 | 12935 | 12915 |
| Suspension second torsion (upper and lower suspensions out of phase) | 12961 | ***13009*** | ***13044*** | 13072 |
| Suspension sway (upper and lower suspensions in phase) | 14033 | 14177 | 14297 | 14352 |
| ***Suspension sway (upper and lower suspensions out of phase)*** | ***14455*** | ***14494*** | ***14600*** | ***14400*** |

Table 3: FEA results for the natural frequencies and mode shapes of the HSA modes that were identified in the experimental measurements.

| Mode Shape | Resonance Frequencies [Hz] | | | |
|---|---|---|---|---|
| | t =1.0 | t =1.2 | t =1.4 | t =1.6 |
| E-block sway coupled with suspension sway | 7450 | 7950 | 8125 | 8325 |
| E-block third torsion coupled with suspension second bending | 9119.5 | 10447 | 11508 | 13421 |
| Suspension second torsion | 12700 | 12200 | 12225 | 12525 |
| ***Suspension sway*** | ***13750*** | ***14100*** | ***14125*** | ***14050*** |

Table 4: Estimates of the frequencies of the three dominant resonant peaks observed in the measured spectra.

| | ID | MD | OD |
|---|---|---|---|
| t = 1.0 | 4.207 | 6.488 | 8.599 |
| t = 1.2 | 5.123 | 7.171 | 9.479 |
| t = 1.4 | 4.346 | 6.016 | 8.228 |
| t = 1.6 | 4.120 | 5.551 | 6.799 |

Table 5: RMS amplitudes [nm] of the slider off-track vibtation over the 2-20 kHz frequency range.

| | ID | MD | OD |
|---|---|---|---|
| t = 1.0 | 1.055 | 1.257 | 1.493 |
| t = 1.2 | 1.140 | 1.336 | 1.738 |
| t = 1.4 | 1.099 | 1.333 | 1.612 |
| t = 1.6 | 1.536 | 1.927 | 2.185 |

Table 6: RMS amplitude components [nm] of the slider off-track vibtation over the 2-6 kHz frequency range.

| | ID | MD | OD |
|---|---|---|---|
| t = 1.0 | 2.549 | 2.363 | 2.783 |
| t = 1.2 | 2.624 | 2.992 | 4.046 |
| t = 1.4 | 3.783 | 4.480 | 5.815 |
| t = 1.6 | 3.091 | 3.146 | 3.873 |

Table 7: RMS amplitude components [nm] of the slider off-track vibtation over the 6-10 kHz frequency range.

| | ID | MD | OD |
|---|---|---|---|
| t = 1.0 | 3.051 | 4.855 | 6.016 |
| t = 1.2 | 3.254 | 5.043 | 6.943 |
| t = 1.4 | 3.273 | 5.436 | 7.308 |
| t = 1.6 | 2.399 | 5.327 | 7.356 |

Table 8: RMS amplitude components [nm] of the slider off-track vibtation over the 10-20 kHz frequency range.

| t [mm] | h [mm] | Re |
|---|---|---|
| 1.0 | 0.5 | 1455 |
| 1.2 | 0.4 | 1164 |
| 1.4 | 0.3 | 873 |
| 1.6 | 0.2 | 582 |

Table 9: Reynolds number at OD for different arm thicknesses.

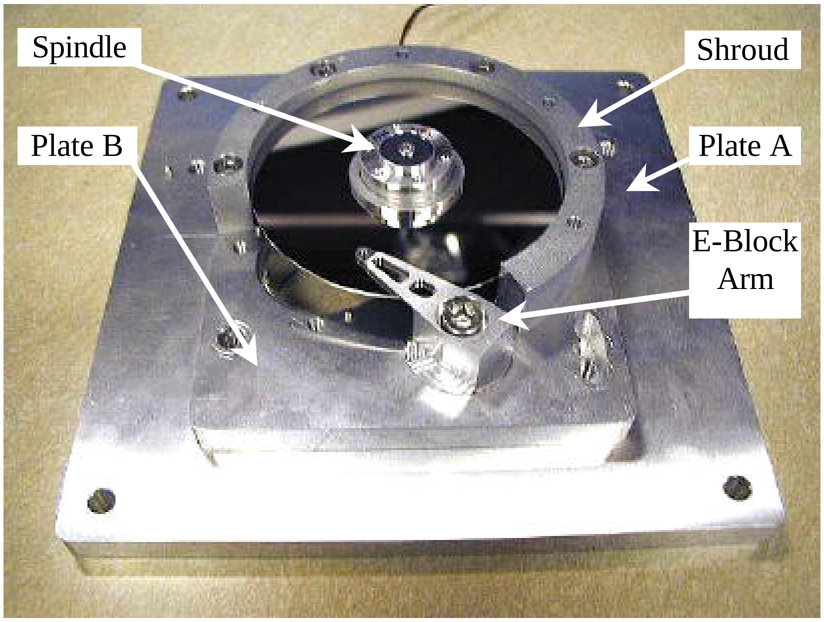


(a) Setup without top disk and cover

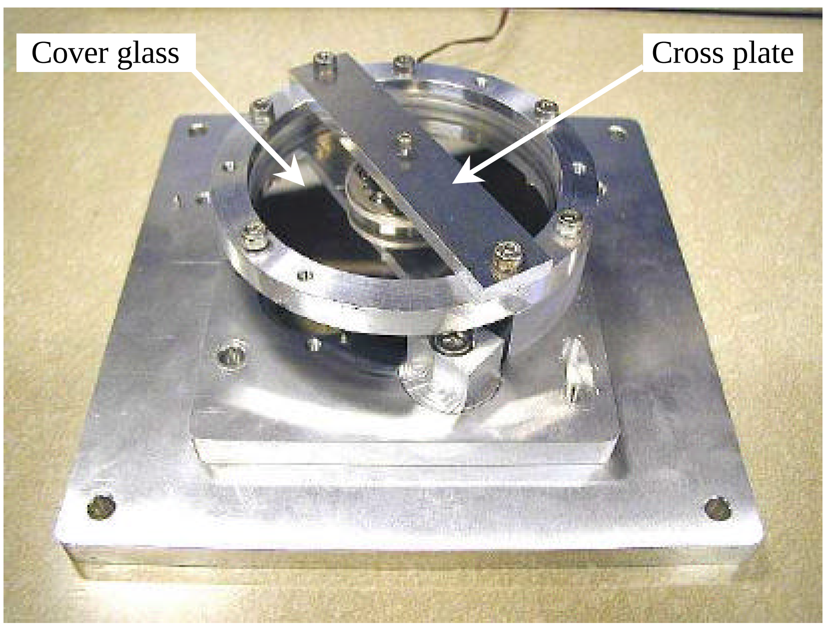


(b) Setup with top disk and cover
Figure 1: Modeled disk drive.

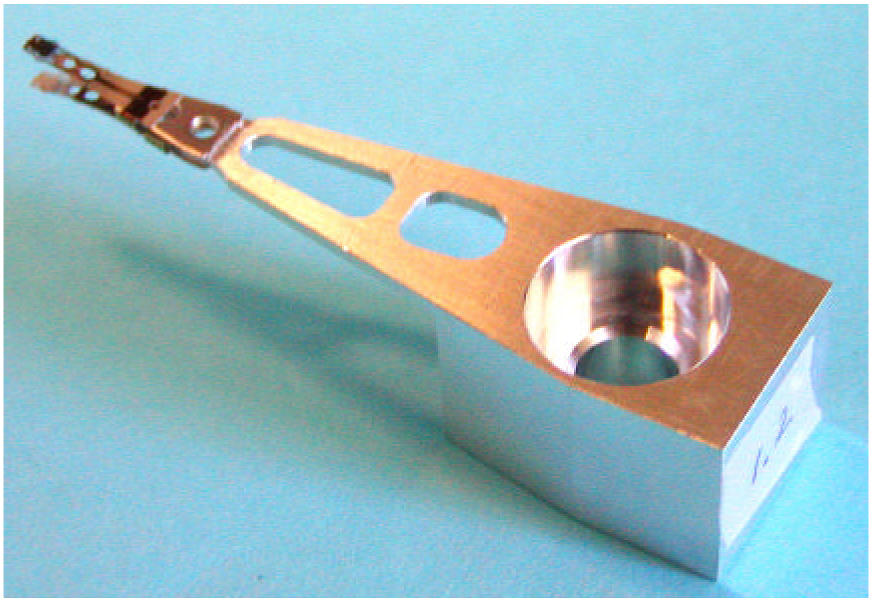

Figure 2: A close-up of the HSA.

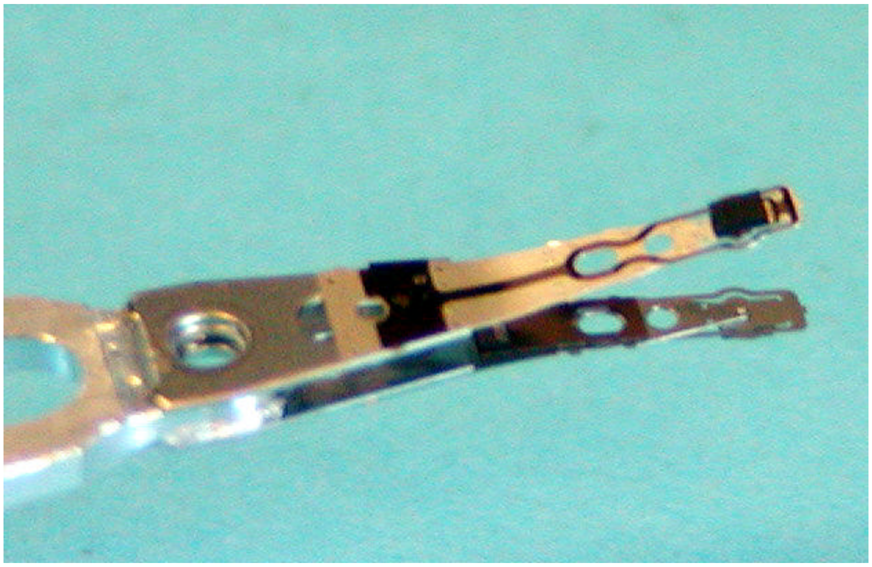

Figure 3: A close-up of the HGA.

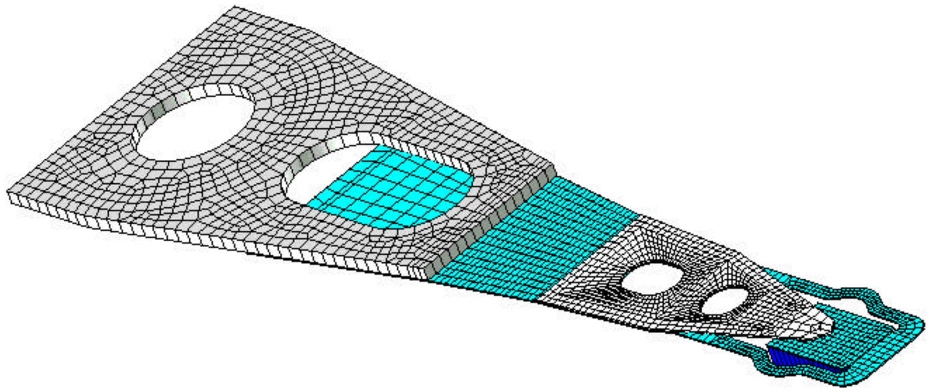

Figure 4: ANSYS model of pico-CAPS HGA.

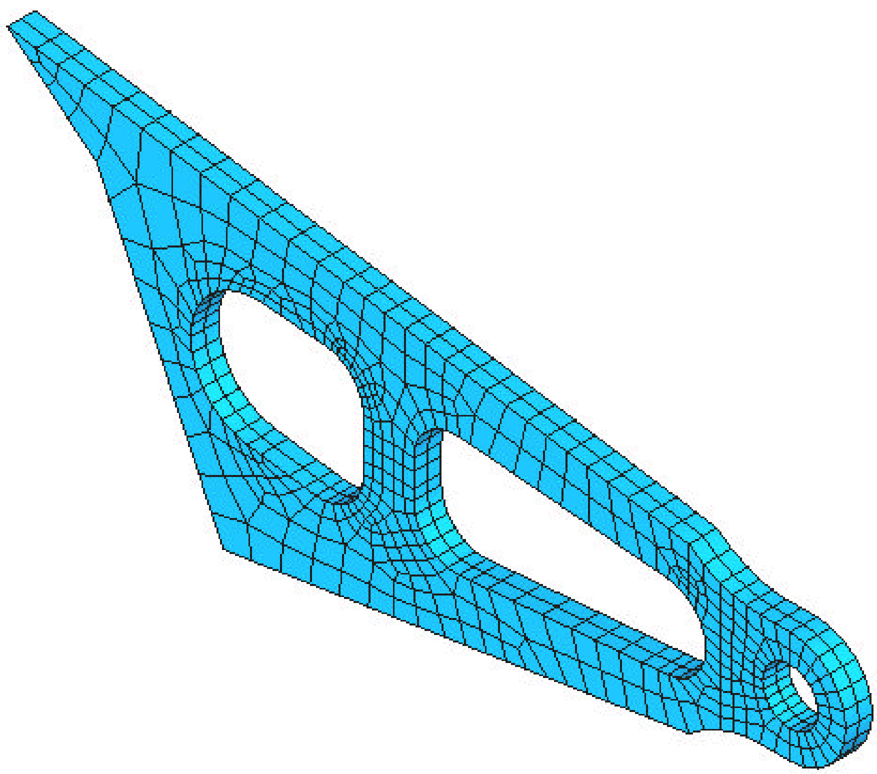

Figure 5: ANSYS model of E-block arm.

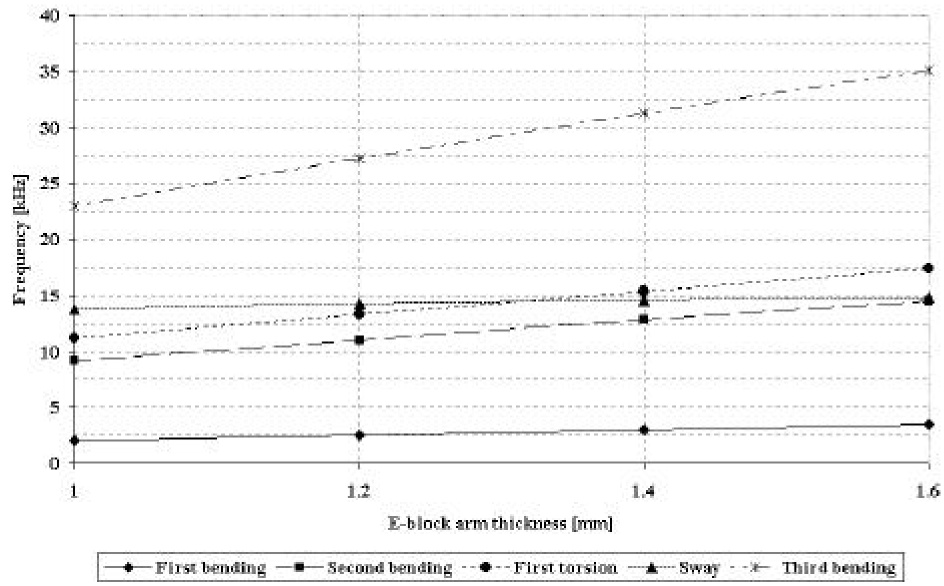


Figure 6: Variation of the natural frequencies of the first five E-block modes as a function of E-block arm thickness.

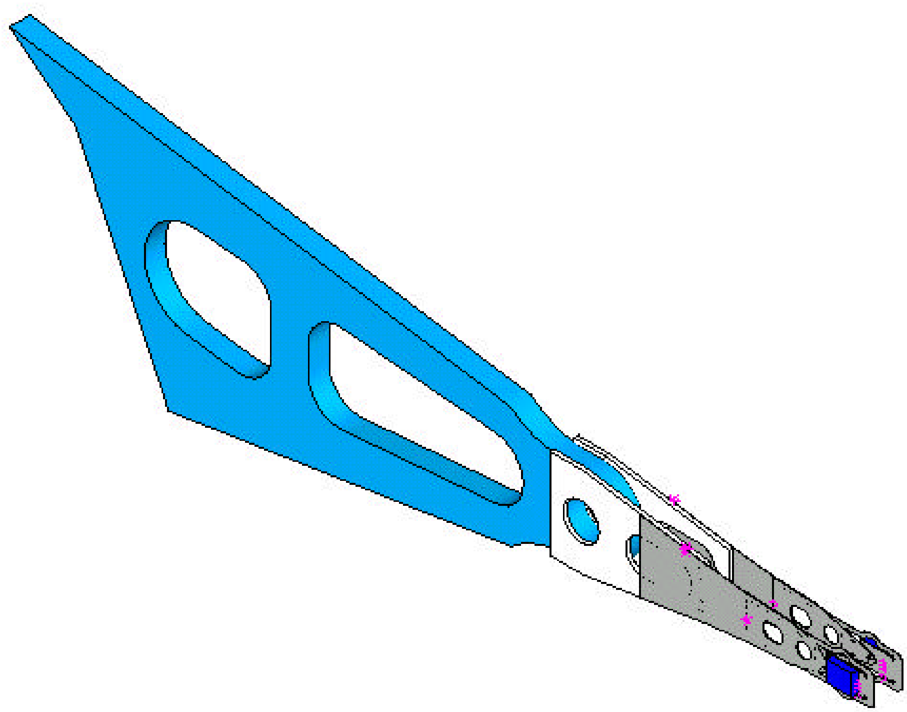

Figure 7: ANSYS HSA model.

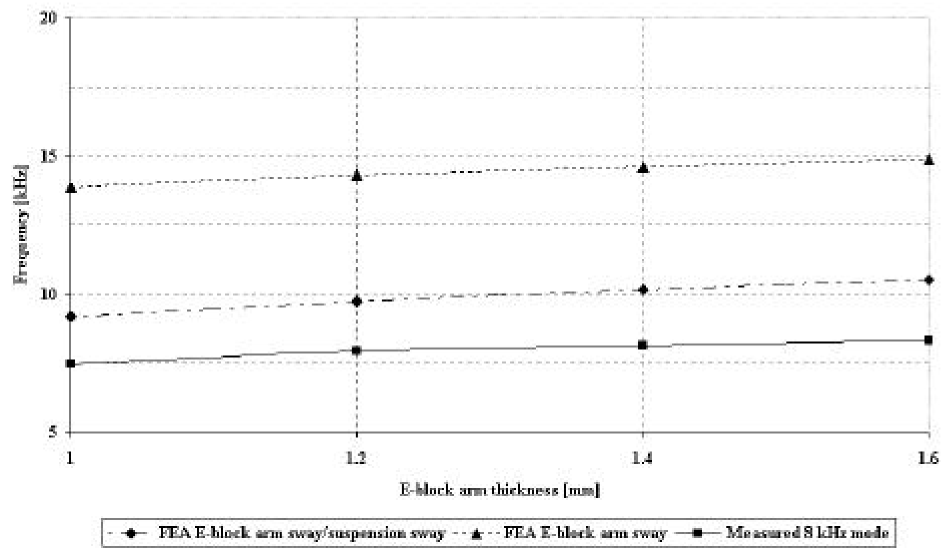


Figure 8: Variation of resonant frequencies of different thickness arms.

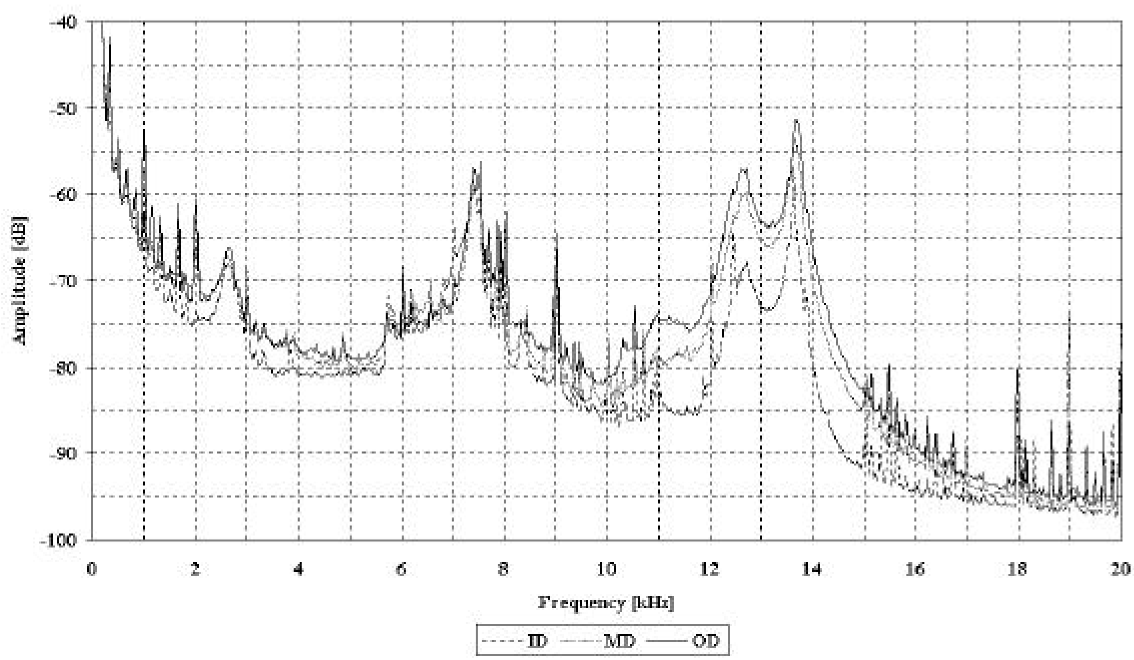


(a) Sample 1

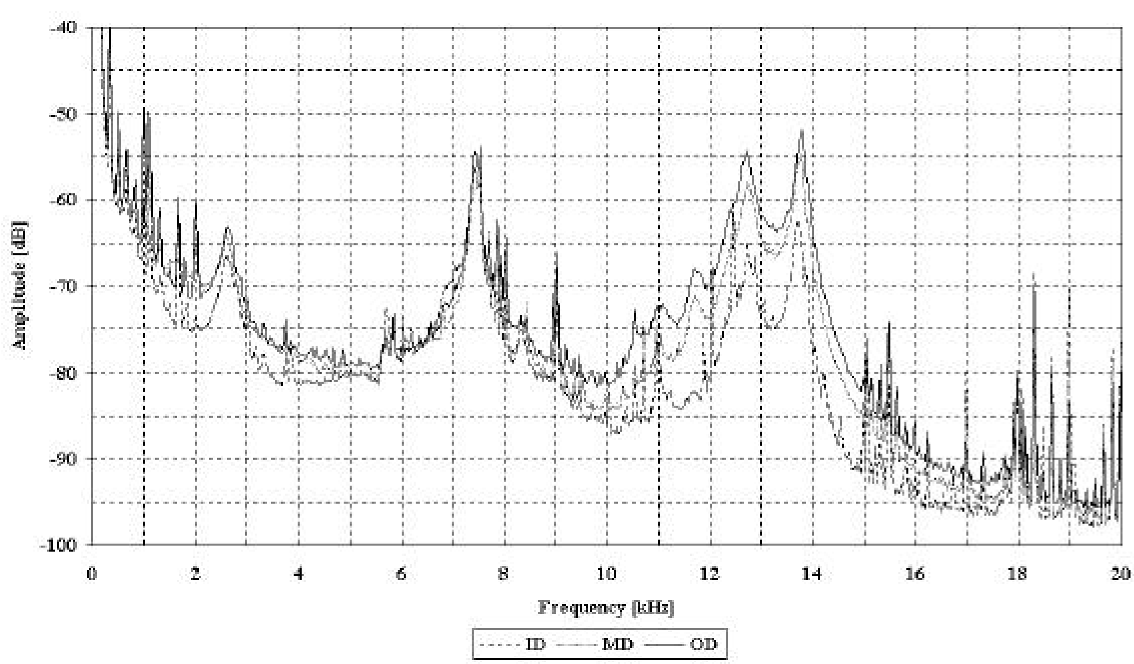


(b) Sample 2

Figure 9: Power spectrum of slider off-track vibration, 1.0 mm thickness arm.

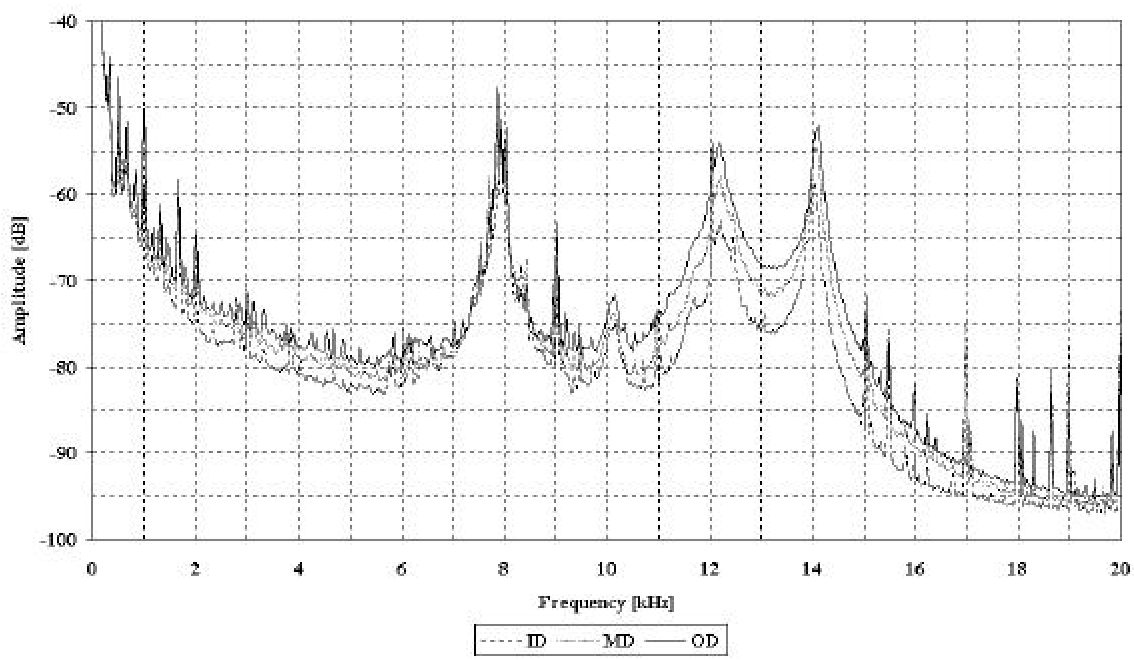


(a) Sample 1

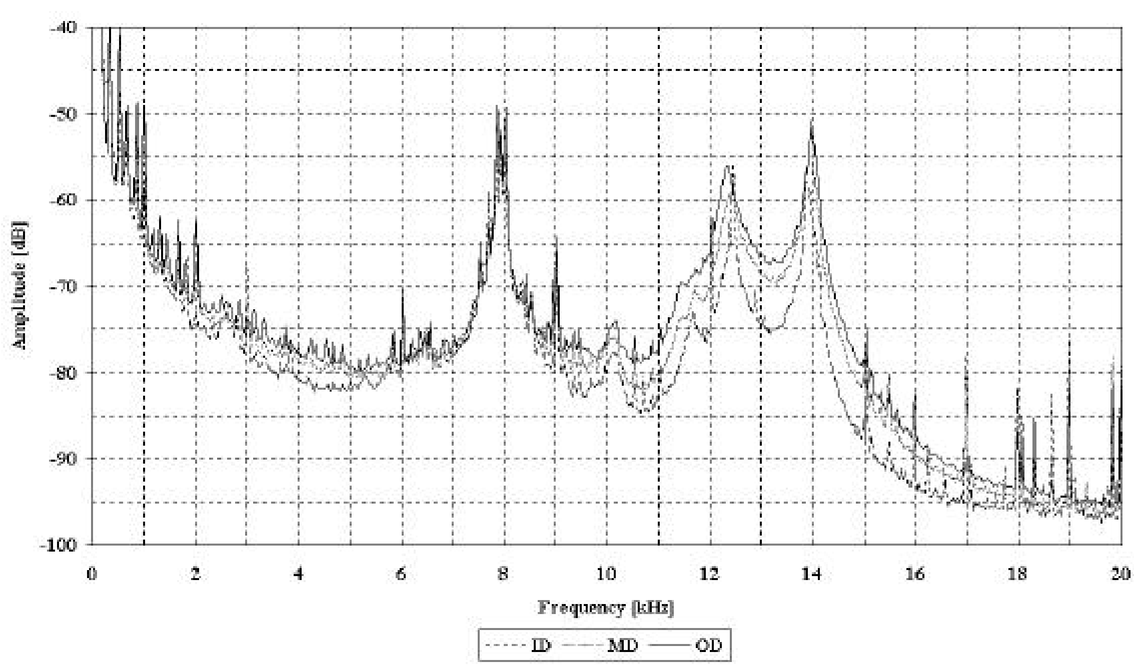


(b) Sample 2

Figure 10: Power spectrum of slider off-track vibration, 1.2 mm thickness arm.

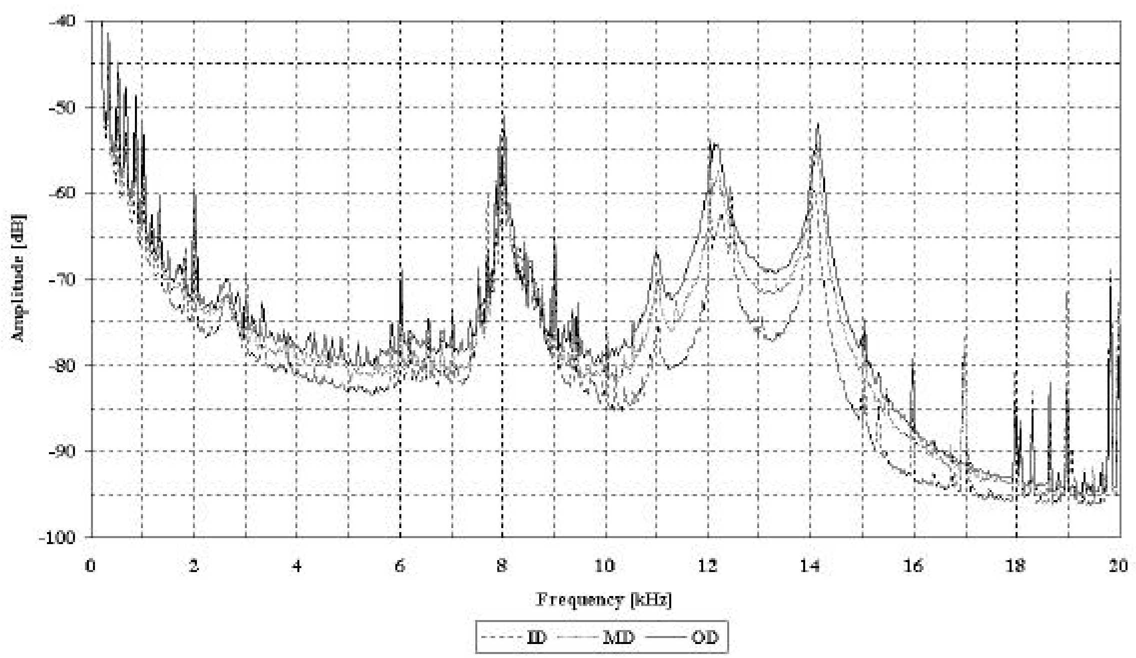


(a) Sample 1

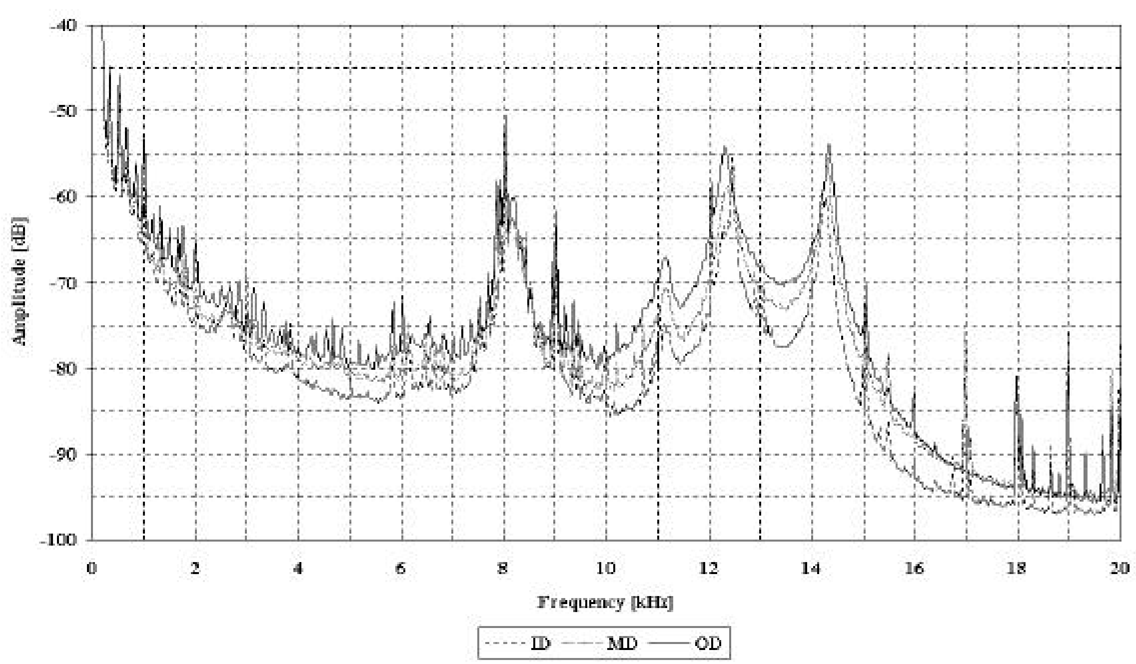


(b) Sample 2

Figure 11: Power spectrum of slider off-track vibration, 1.4 mm thickness arm.

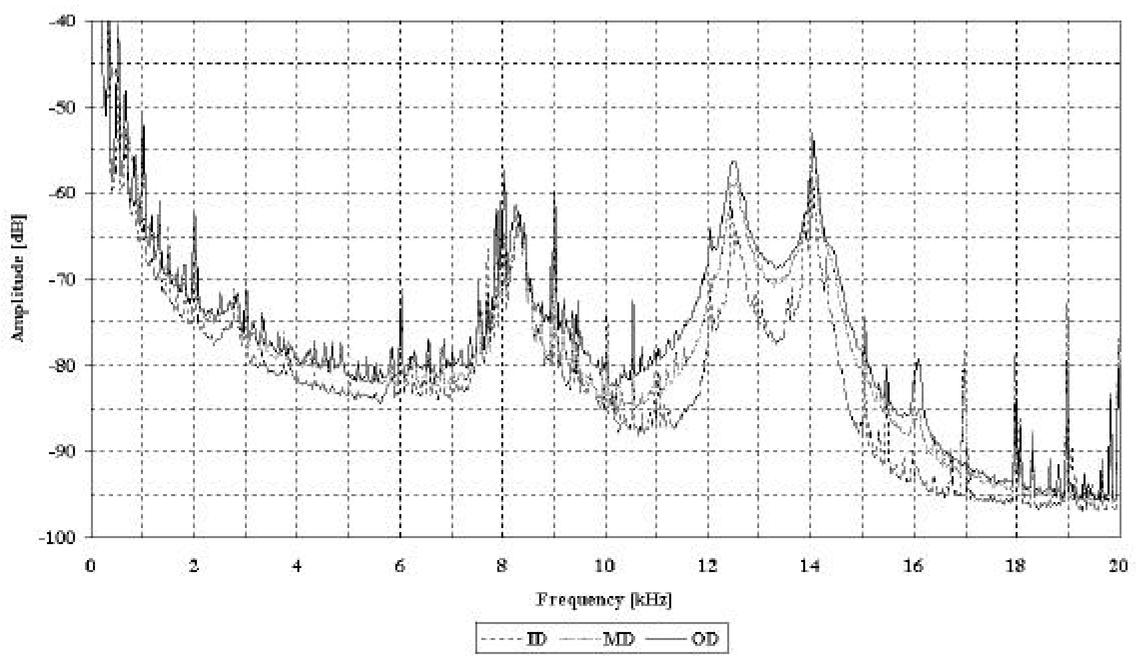


(a) Sample 1

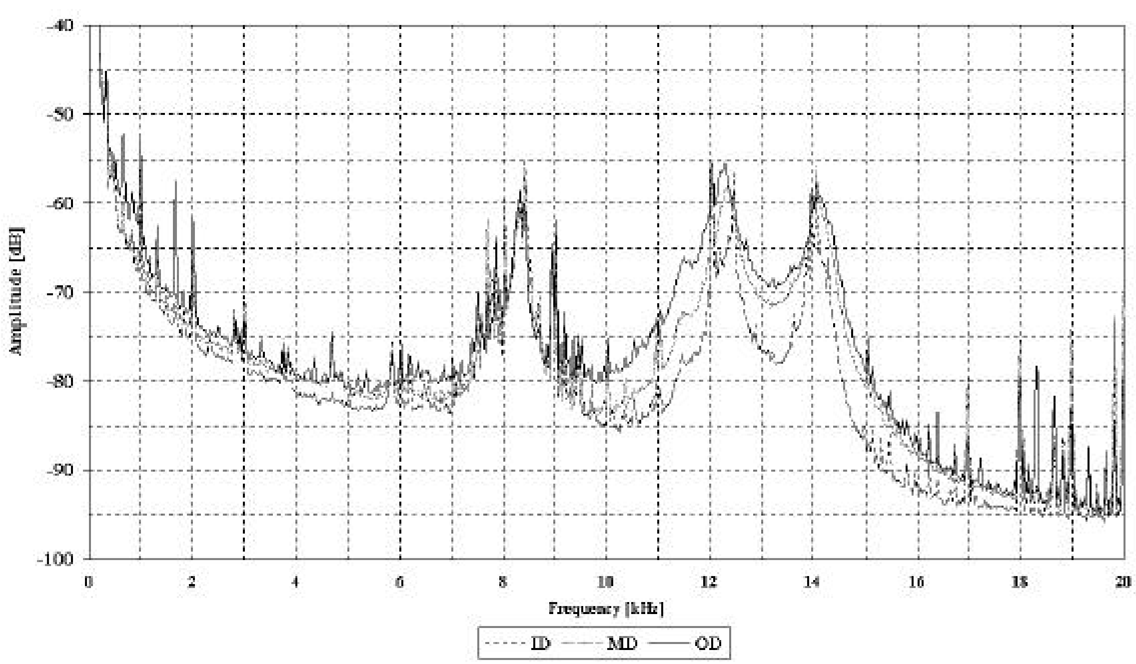


(b) Sample 2

Figure 12: Power spectrum of slider off-track vibration, 1.6 mm thickness arm.

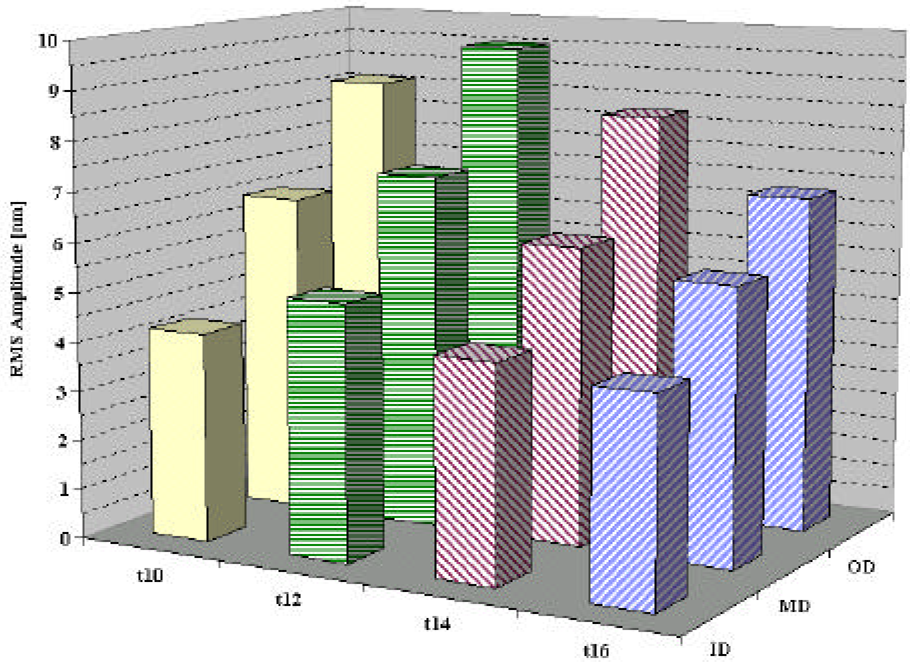


Figure 13: RMS amplitudes [nm] of the slider off-track vibration over the 2-20 kHz frequency range.

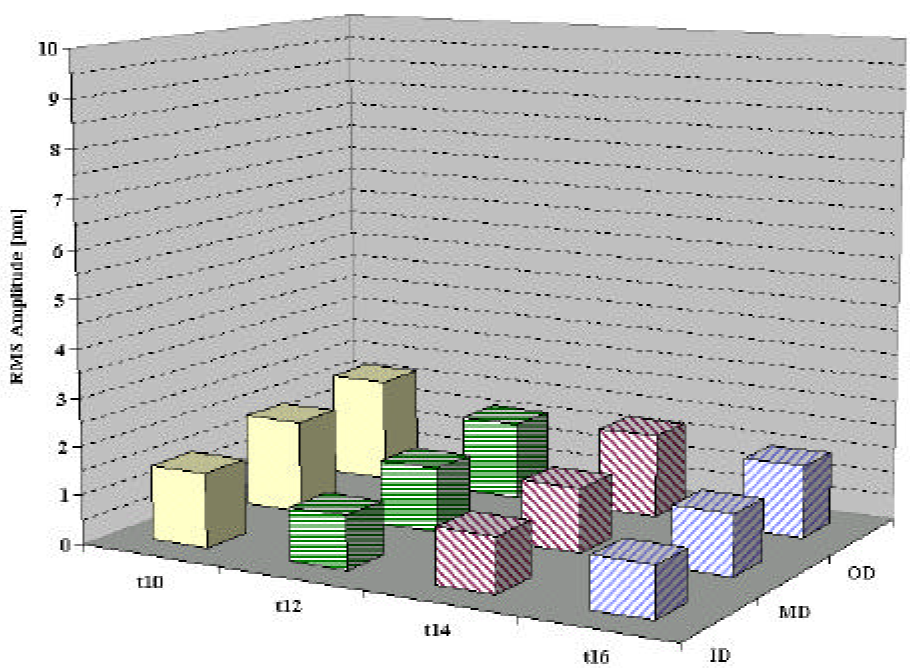


Figure 14: RMS amplitude component [nm] of the slider off-track vibration over the 2-6 kHz frequency range.

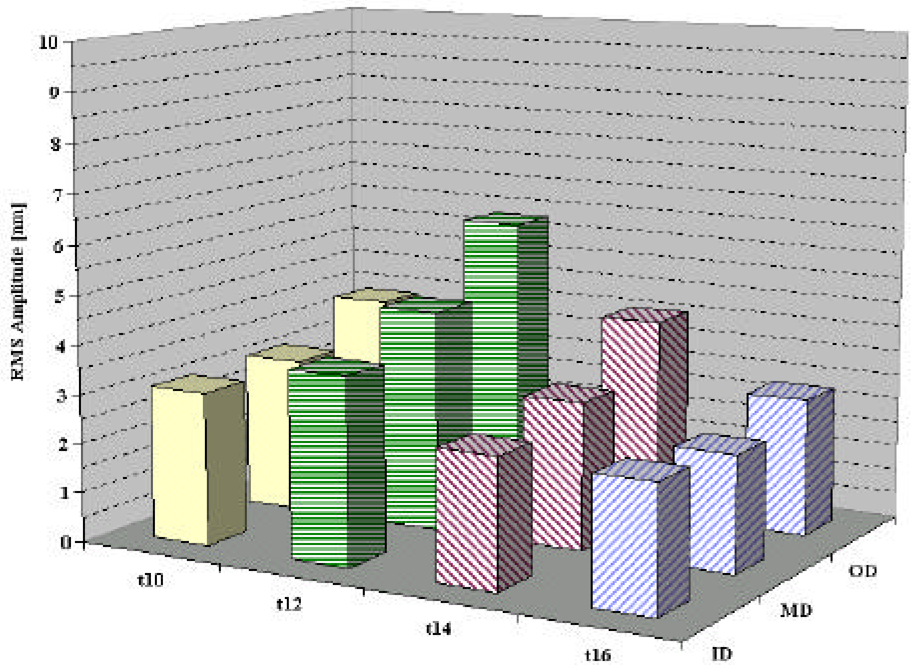


Figure 15: RMS amplitude component [nm] of the slider off-track vibration over the 6-10 kHz frequency range.

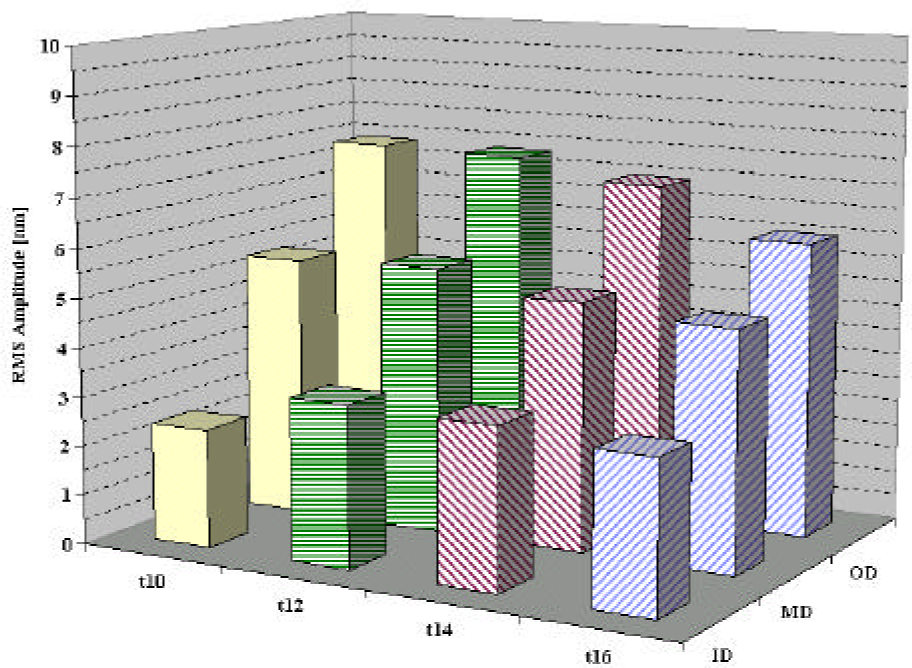


Figure 16: RMS amplitude component [nm] of the slider off-track vibration over the 10-20 kHz frequency range.